INTERNATIONAL JOURNAL FOR NUMERICAL METHODS IN FLUIDS, VOL. 11, 189–207 (1990)

# FINITE VOLUME MULTIGRID PREDICTION OF LAMINAR NATURAL CONVECTION: BENCH-MARK SOLUTIONS

M. HORTMANN AND M. PERIĆ

*Lehrstuhl für Strömungsmechanik, Egerlandstraße 13, D-8520 Erlangen, F.R.G.*

AND

G. SCHEUERER

*Gesellschaft für Reaktorsicherheit mbH, Forschungsgelände, D-8046 Garching, F.R.G.*

## SUMMARY

A finite volume multigrid procedure for the prediction of laminar natural convection flows is presented, enabling efficient and accurate calculations on very fine grids. The method is fully conservative and uses second-order central differencing for convection and diffusion fluxes. The calculations start on a coarse (typically $10 \times 10$ control volumes) grid and proceed to finer grids until the desired accuracy or maximum affordable storage is reached. The computing times increase thereby linearly with the number of control volumes.

Solutions are presented for the flow in a closed cavity with side walls at different temperatures and insulated top and bottom walls. Rayleigh numbers of $10^4$, $10^5$ and $10^6$ are considered. Grids as fine as $640 \times 640$ control volumes are used and the results are believed to be accurate to within 0·01%. Second-order monotonic convergence to grid-independent values is observed for all predicted quantities.

KEY WORDS Finite volume Multigrid Numerical accuracy Natural convection Bench-mark solution

## 1. INTRODUCTION

The prediction of complex flows requires the use of very fine grids if high numerical accuracy is demanded. However, standard iterative finite difference (FD) and finite volume (FV) methods are known to converge more and more slowly as the grid is refined: the number of iterations required for convergence increases typically linearly, and computing time therefore quadratically. Computations on grids with more than 100 points in one space direction are hence extremely expensive, and are yet in many instances not accurate enough.

More accurate results can be obtained by using Richardson extrapolation if solutions on at least two consecutive grids are available, as done by de Vahl Davis.[1] However, for this extrapolation to be accurate it is necessary that the two grids employed are fine enough to guarantee monotonic convergence with a known order, which again may be difficult to satisfy (see the discussion by de Vahl Davis[1] about calculations for Rayleigh number $10^6$).

In recent years multigrid FD and FV methods applicable to the solution of coupled non-linear equations were developed; see e.g. References 2–8. The application of the multigrid idea results in

0271–2091/90/100189–19$09.50

*Received August 1989*

an approximately linear increase of computing time with grid refinement, allowing much finer grids to be used and therefore more accurate solutions to be obtained. In this paper an extension of the FV multigrid approach with collocated grids developed by Becker *et al.*[7] to buoyant laminar flows is presented.

In the next section the basic FV method is briefly described, followed by the description of the superimposed multigrid technique. The bench-mark solutions for the flow in a closed cavity with heat transfer through the side walls are then presented. In the final section the most important findings of this study are summarized.

## 2. DISCRETIZATION METHOD

The conservation equations, governing the transport of mass, momentum and heat, are

$$\frac{\partial}{\partial x_j}(\rho U_j)=0, \tag{1}$$

$$\frac{\partial}{\partial x_j}\left(\rho U_j U_i-\mu\frac{\partial U_i}{\partial x_j}\right)=-\frac{\partial P}{\partial x_i}+\frac{\partial}{\partial x_j}\left[\mu\left(\frac{\partial U_j}{\partial x_i}\right)\right]+(\rho-\rho_0)g_i, \tag{2}$$

$$\frac{\partial}{\partial x_j}\left(\rho U_j T-\frac{\mu}{Pr}\frac{\partial T}{\partial x_j}\right)=0. \tag{3}$$

Here $\rho$ is the density, $U_i$ and $x_i$ are the Cartesian velocity components and co-ordinate directions respectively, $T$ is the temperature, $Pr$ is the Prandtl number, $\mu$ is the dynamic viscosity and $g_i$ is the component of the gravity acceleration vector in the $x_i$-direction. The subscript '0' denotes reference mean values. The second term on the right-hand side of (2) vanishes when $\mu$ and $\rho$ are constant. If the Boussinesq approximation is applied, the last term becomes

$$(\rho-\rho_0)g_i=\rho_0 g_i\beta(T-T_0), \tag{4}$$

where $\beta$ is the coefficient of thermal expansion and $T_0$ is the reference temperature at which $\mu$, $Pr$ and $\rho_0$ are defined.

The transport equations are integrated over a finite number of control volumes (CVs), leading to balance equations of fluxes $F$ through the CV faces, and volumetric sources $S$. Thus (see Figure 1 for the grid arrangement and notation)

$$F_e-F_w+F_n-F_s=S. \tag{5}$$

Evaluation of the convection and diffusion contribution to the flux $F$ will be described for the CV face 'w'; analogous expressions follow for the other faces.

First the cell face mass flux is evaluated as

$$\dot{m}_w=(\rho U\delta y)_w, \tag{6}$$

where $U_w$ is taken to represent the mean value over the CV face; it is calculated by using an interpolation formula appropriate for the collocated variable arrangement used here. Details on this practice are given by Perić *et al.*[10] The mass fluxes are assumed to be known when solving the momentum and heat transport equations.

The convective flux of a variable $\phi$ is evaluated as

$$F_w^C=\dot{m}_w\phi_w, \tag{7}$$

where $\phi_w$ stands for the mean value of the transported variable ($U_i$ or $T$) at the CV face 'w'. The

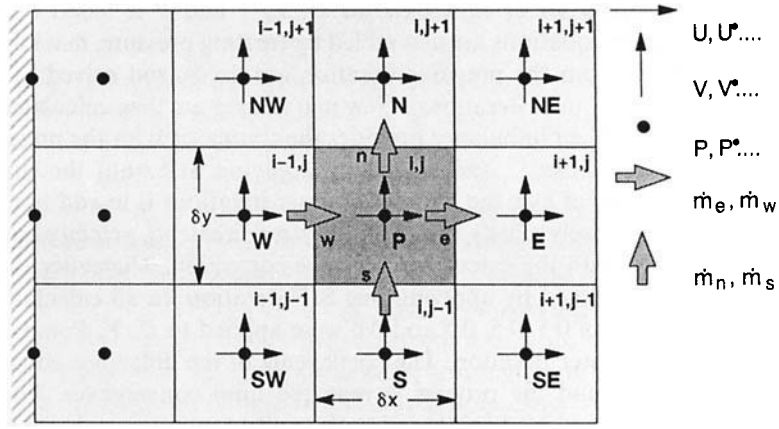


Figure 1. Computational grid and labelling scheme

estimate for this value is expressed in terms of the nodal values by employing the central differencing scheme (CDS), which implies linear interpolation between nodes W and P. CDS is implemented in the solution procedure using the deferred correction approach suggested by Khosla and Rubin.[11]

The diffusion flux involves an estimate of the mean gradient of $\phi$ at the CV face. Here again CDS is employed, leading to

$$F_w^D = -\frac{\mu}{Pr}\frac{\phi_P - \phi_W}{x_P - x_W}\delta y_w. \tag{8}$$

Note that for CVs next to boundaries of the solution domain (see Figure 1) the convected value $\phi_w$ is the boundary value, and the gradient expression in (8) reverts to two-point backward or forward differencing. The latter is, however, supposed to be equally accurate as the CDS expression for the interior CV faces, since the distance between the two nodes involved is typically halved. The accuracy is further increased by using non-uniform grids which are finer near boundaries, as will be discussed later.

The sources are integrated over the cell volume. This is done by evaluating the specific source at the central point P, which is then taken to represent the mean value over the whole CV—hence the integration involves only multiplication of the nodal value by the cell volume (note that the point P resides in the centre of the CV). The source of $U$-momentum becomes then

$$S_u = -\delta y(P_e - P_w) + \rho_0 g_x \beta (T_P - T_0)\delta x \delta y. \tag{9}$$

Finally, (5) can be rewritten as an algebraic equation of the form

$$A_P \phi_P + \sum_{nb} A_{nb}\phi_{nb} = S_\phi, \tag{10}$$

where nb = E, W, N, S are the four immediate neighbours of point P, and $\phi$ stands for $U$, $V$ or $T$. For the solution domain as a whole, a matrix equation

$$[A]\{\phi\} = \{S\} \tag{11}$$

results. The strongly implicit procedure (SIP) of Stone[12] is used to relax this equation to a prescribed tolerance on all grids.

The solution of the coupled set of equations for $U$, $V$, $T$ and $P$ is based on the SIMPLE algorithm.[13] The momentum equations are assembled by treating pressure, mass fluxes and other variables as known (values from the previous iteration are used), and solved by applying one iteration of the SIP algorithm (inner iterations). New mass fluxes are then calculated based on the just calculated velocity field. Their imbalance provides the source term for the pressure correction equation, which is then assembled[10] and solved by applying SIP until the sum of absolute residuals has fallen by a factor of five; the number of inner iterations is in addition limited to 15. The mass fluxes (they now closely satisfy the continuity requirement), velocity components and pressure are then corrected with the calculated pressure correction. Thereafter the temperature equation is assembled and relaxed by applying one SIP iteration. In all calculations presented here, underrelaxation factors of 0·5, 0·5, 0·5 and 0·6 were applied to $U$, $V$, $P$ and $T$ respectively.

The above describes one outer iteration. The coefficients of the difference equations are then updated and solved in turn and the process is repeated until convergence. The convergence criterion used here is that the sum of absolute residuals in all equations is reduced by at least four orders of magnitude. This assures that the solution does not change in the four most significant figures. This was checked by performing calculations in which one further order of residual reduction was demanded.

In the present multigrid procedure the described solution strategy is applied on all grid levels, the only difference being that the coarse grid equations contain additional source terms, as will be described in the next section.

## 3. MULTIGRID METHOD

The rate of convergence of the above solution method is highest at the beginning of the calculation; it becomes worse after a few outer iterations, the effect being more pronounced as the grid is refined. The reason is that the iterative solution procedure used removes efficiently only those Fourier components of the error whose wavelengths are smaller than or comparable to the grid spacing. The multigrid procedure aims at covering a wider spectrum of wavelengths by iterating on various grids, so that on each grid the corresponding error components are efficiently damped.

The exact solution for any variable on grid $k$, $\Phi_k$, satisfies the equation

$$[\mathscr{A}_k]\{\Phi_k\} = \{\mathscr{S}_k\} \tag{12}$$

where $[\mathscr{A}_k]$ and $\{\mathscr{S}_k\}$ are the coefficient matrix and source term vector for the variable in question, based on the exact solutions on grid $k$ of the coupled variables.

After $v_k^t$ outer iterations, approximate solutions $\phi_k$ are obtained satisfying the following equation:

$$[A_k]\{\phi_k\} = \{S_k\} - \{R_k\}. \tag{13}$$

$[A_k]$ and $\{S_k\}$ are approximations to $[\mathscr{A}_k]$ and $\{\mathscr{S}_k\}$ based on the approximate solutions $\phi_k$, and $\{R_k\}$ are the residuals (the difference between the left- and right-hand sides of (10), computed with the updated coefficients and prevailing variable values).

Subtracting (13) from (12) yields

$$[\mathscr{A}_k]\{\Phi_k\} = \{\mathscr{S}_k\} + [A_k]\{\phi_k\} - \{S_k\} + \{R_k\}. \tag{14}$$

This equation is used as the basis for multigrid coupling. We assemble an approximation to the above equation on the next coarser grid, $k-1$, as follows:

$$[\hat{A}_{k-1}]\{\hat{\phi}_{k-1}\} = \{\hat{S}_{k-1}\} + \underline{[\tilde{A}_{k-1}]\{\tilde{\phi}_{k-1}\} - \{\tilde{S}_{k-1}\} + \{\tilde{R}_{k-1}\}}. \tag{15}$$

Variables and operators on grid $k-1$ based on the current approximate solution on the finer grid $k$ are denoted by ($\tilde{}$), and variables and operators being modified in the course of iterations on the coarser grid $k-1$ by ($\hat{}$). The latter are also to be distinguished from the variables and operators obtained on grid $k-1$ when it is the current finest grid.

In the FV method used here it is advantageous to build the coarser grid CVs by putting together four fine grid CVs as shown in Figure 2. When a collocated variable arrangement is used, only one set of CVs needs to be coarsened, and both fine and coarse grids fit the boundaries of the solution domain, which is a great advantage in comparison with the staggered variable arrangement. The storage locations on the two grids do not coincide (see Figure 2) and therefore the transfer of variable values from fine ($k$) to coarse ($k-1$) grid has to be performed by interpolation (restriction). For this purpose bilinear interpolation, denoted by the operator $I_k^{k-1}$, is employed; thus

$$\tilde{\phi}_{k-1} = I_k^{k-1}\,\phi_k. \tag{16}$$

Note that the difference equations in the FV method represent balances of fluxes through the CV faces and over volume-integrated sources; thus the coarse grid balance equation is equal to the sum of the four balance equations for the corresponding fine grid CVs (see Figure 2). Therefore the transfer of residuals requires no interpolation, since (see Figure 3)

$$\tilde{R}_{k-1}^{I,J} = R_k^{i,j} + R_k^{i,j+1} + R_k^{i+1,j} + R_k^{i+1,j+1}. \tag{17}$$

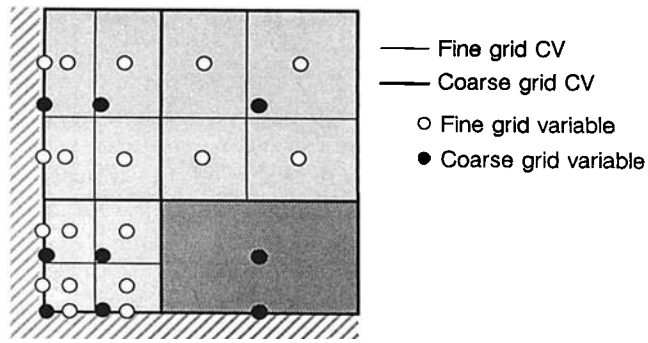


Figure 2. Grid refinement and storage locations

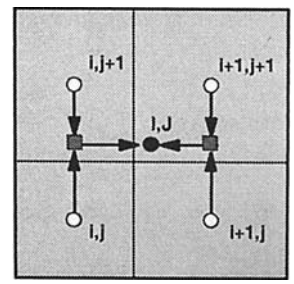


Figure 3. Schematic presentation of restriction

Although it would seem appropriate to evaluate $\tilde{S}_{k-1}$ in the same way, this is not done for consistency reasons; namely, it has to be ensured that the coarse grid equations become identically satisfied, i.e. $\hat{\phi}_{k-1} = \tilde{\phi}_{k-1}$ (no correction) when $R_k$ equals zero. For this reason $\tilde{S}_{k-1}$ is assembled on the coarse grid in the same way as $\hat{S}_{k-1}$ but using $\tilde{\phi}_{k-1}$-values where dependence on $\phi$ occurs. Since the starting values for $\hat{\phi}_{k-1}$ are $\tilde{\phi}_{k-1}$, the source terms $\hat{S}_{k-1}$ and $\tilde{S}_{k-1}$ are identical in the first coarse grid iteration and thus the above requirement is met. Analogously $[\tilde{A}_{k-1}]$ is assembled on the coarse grid in the same way as $[\hat{A}_{k-1}]$, and the two operators are also identical in the first coarse grid iteration. However, the initial mass fluxes on the coarse grid, which are used to assemble the coefficients $A$ (see equation (10)), are conservatively evaluated by summing the fine grid mass fluxes through the corresponding CV faces (see Figure 4). Thus when the fine grid mass fluxes satisfy the continuity equation, this is automatically ensured on the coarse grid too. The coarse grid mass fluxes will only be corrected in the course of coarse grid iterations by the difference between the values of $\hat{U}_{k-1}$ and $\tilde{U}_{k-1}$, $\hat{V}_{k-1}$ and $\tilde{V}_{k-1}$ according to equation (6). Since the pressure operator is linear, on the coarse grid, we need to calculate only a *correction* to the fine grid pressure. The pressure correction equation produces a correction to the above correction while iterating on the coarse grid (each time starting from zero initial values).

The underlined terms in (15) are calculated once and then kept unchanged during iterations on the coarse grid; they appear as extra source terms in equation (10). If the fine grid residuals $R_k$ are significant, the $\hat{\phi}_{k-1}$-values will in the course of $\nu^r_{k-1}$ iterations depart from their initial values $\tilde{\phi}_{k-1}$. The difference represents the correction to the fine grid solution $\phi_k$ calculated on the coarse grid. In order to apply the correction, it has to be extrapolated (prolongated) from the coarse to the fine grid. Bilinear interpolation, denoted by $I^k_{k-1}$, is used here. The updated fine grid variable is then (see Figure 5)

$$\phi_k^{\text{new}} = \phi_k^{\text{old}} + I^k_{k-1}(\hat{\phi}_{k-1} - \tilde{\phi}_{k-1}). \tag{18}$$

The above describes one V-cycle on two grids. In practice more than two grids are employed; in this case, after $\nu^r_{k-1}$ iterations on grid $k-1$ the approximate solution $\hat{\phi}_{k-1}$ will be transferred to the coarser grid $k-2$ and used there as $\tilde{\phi}_{k-2}$, and so on. When the coarsest grid is reached, the reverse procedure starts, in which corrections are evaluated and transferred to the finer grid. These are added to the prevailing variable values there, and after $\nu^p_k$ iterations (required to smooth the high-frequency errors due to interpolation) the corrections for the finer grid are evaluated and transferred, and so on, until the finest grid is reached.

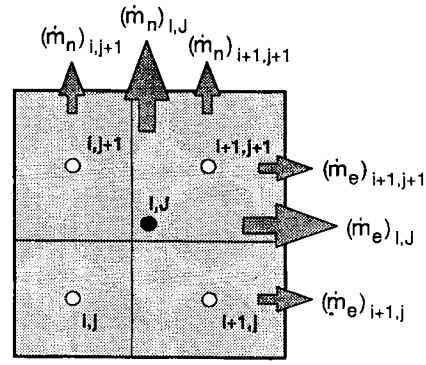


Figure 4. Restriction of mass fluxes

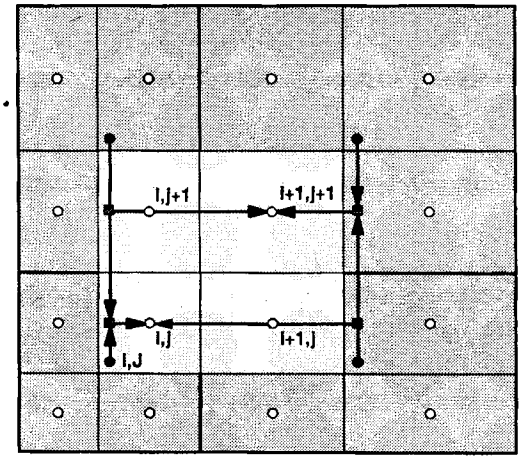


Figure 5. Schematic presentation of prolongation

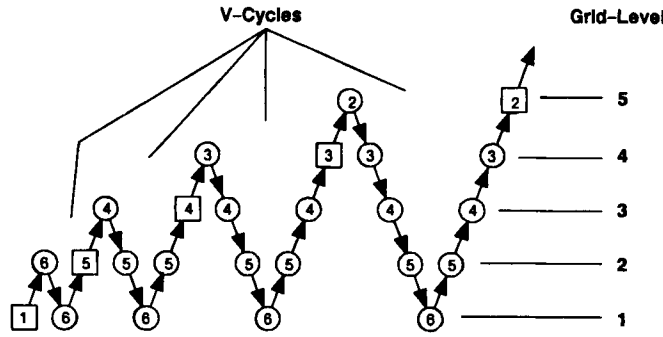


Figure 6. Schematic presentation of the FMG procedure used; numbers indicate SIMPLE iterations on one grid level

We have implemented our multigrid procedure in a so-called 'full multigrid' (FMG) fashion, as was also done by Becker *et al.*[7] and Perić *et al.*[8] First the solution is obtained on the coarsest grid (typically 10 × 10 CV). This solution is then extrapolated to the next finer grid 2 and used there as a starting guess for the V-cycle multigrid procedure. When grid 2 is done, the solution is transferred to grid 3 and so on (see Figure 6). The advantage of this strategy as compared to starting the solution process on the finest grid is that it allows for the evaluation of the numerical accuracy of the solution on each refined grid, by comparing it to the solution on the next coarser grid.[7] Also better solution estimates may be obtained by using Richardson extrapolation if the solutions on several grids are known. The cost of obtaining the coarser grid solutions is covered by the savings on the finest grid due to having good initial guesses for all variables.

In a multigrid procedure for single equations the convergence rate (determined by the ratio of residual norms after two successive iterations) is monitored and used as a criterion for deciding when to switch from one grid to another.[2] With a coupled system of equations (here four: for $U$, $V$, $P$ and $T$) this practice is not easy to implement, since the rate of convergence of the various equations may differ and not necessarily be always monotonic. We have therefore specified fixed

numbers of $\nu^r$ (down or restrict) and $\nu^p$ (up or prolong) iterations in the V-cycle without attempting to optimize them. These are indicated in Figure 6, which represents the FMG–FAS scheme used in our calculations. Other authors have also found this practice to be sometimes more efficient than a dynamic criterion.

## 4. RESULTS OF CALCULATIONS

Flow in a square cavity with insulated top and bottom walls and with side walls maintained at constant but different temperature (see Figure 7) is often used for testing numerical solution methods.[1,9] A bench-mark solution for this problem has been published by de Vahl Davis.[1] He used a streamfunction–vorticity FD method with grids up to 81 × 81 points, and employed Richardson extrapolation to obtain more accurate bench-mark solutions for Rayleigh numbers ($Ra$) up to $10^6$. In this paper multigrid calculations for $Ra = 10^4$, $10^5$ and $10^6$, with grids as fine as 640 × 640 CV, are presented.

Starting with the coarsest grid of 10 × 10 CV, the grids were refined until the difference between the mean Nusselt numbers calculated on the two finest grids was lower than 0·02%. Table I shows the fluid properties and cavity dimensions used in the calculations.

Both uniform (square) and non-uniform grids were employed. The latter had the smallest mesh size near walls and the largest at the centre. The smallest $\delta x$ on the 10 × 10 CV non-uniform grids was taken to be 1/20 of the cavity width (i.e. the same as on a 20 × 20 CV uniform grid); the spacing was then increased by a constant factor (expansion ratio) $\eta_1 = 1{\cdot}352$, i.e.

$$\delta x_i = \eta_1 \delta x_{i-1}. \tag{19}$$

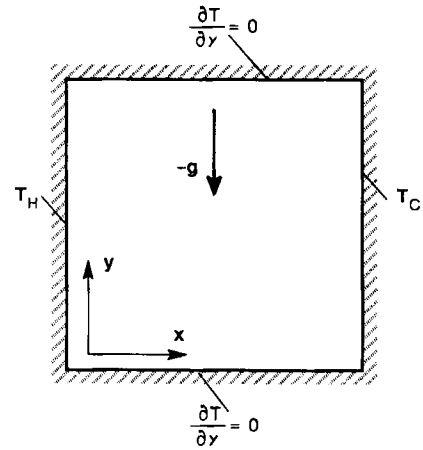


Figure 7. Geometry of the test case and boundary conditions

Table I. Fluid properties and cavity dimensions used in calculations

| $Ra$ | $\rho$ | $\mu$ | $\beta$ | $Pr$ | $g$ | $T_H$ | $T_C$ | $L$ | $H$ |
|---|---|---|---|---|---|---|---|---|---|
| $10^4$ | 1·19 | $1{\cdot}8 \times 10^{-5}$ | 0·00341 | 0·71 | 9·81 | 12 | 2 | 0·021277 | 0·021277 |
| $10^5$ | 1·19 | $1{\cdot}8 \times 10^{-5}$ | 0·00341 | 0·71 | 9·81 | 12 | 2 | 0·045841 | 0·045841 |
| $10^6$ | 1·19 | $1{\cdot}8 \times 10^{-5}$ | 0·00341 | 0·71 | 9·81 | 12 | 2 | 0·098761 | 0·098761 |

The coarser grids were subsets of the finer grids; each coarse grid cell width $\delta x$ was divided in two parts, keeping the expansion factor constant. The latter becomes smaller as the grid gets finer, according to

$$\eta_k = \sqrt{\eta_{k-1}}. \tag{20}$$

Thus the finest grid with 640 × 640 CV was almost uniform, with $\eta_7 = 1{\cdot}0047$; however, the smallest $\delta x$ on this grid was equal to $L/1490$. Table II shows the smallest grid spacing as a fraction of cavity width on various grids (distribution of grid lines in the $x$- and $y$-direction is the same). Figure 8 shows segments of the first four grids (one quarter of each). Note that the grid lines (CV boundaries) of the coarse grid remain also grid lines of the fine grid, i.e. one coarse grid CV makes up exactly four CVs of the refined grid. This is an important feature of the present multigrid method which enables the conservation principle to be retained on all grid levels, as noted in the previous section.

Streamlines and isotherms predicted on the finest grids for flows at $Ra = 10^5$ and $10^6$ are presented in Figures 9(a)–9(d). These show typical features of such flows known from the literature.[1] Little difference could be observed visually between such plots obtained on grids 80 × 80 and finer. However, quantitative differences do exist, as will be discussed below.

Table II. Smallest $\delta x$ as a fraction of cavity width for various grids

| Grid: | 10 × 10 | 20 × 20 | 40 × 40 | 80 × 80 | 160 × 160 | 320 × 320 | 640 × 640 |
|---|---|---|---|---|---|---|---|
| Uniform | 0·1 | 0·05 | 0·025 | 0·0125 | 0·00625 | 0·003125 | 0·0015625 |
| Non-uniform | 0·05 | 0·023117 | 0·011122 | 0·0054561 | 0·0027024 | 0·0013448 | 0·000672 |

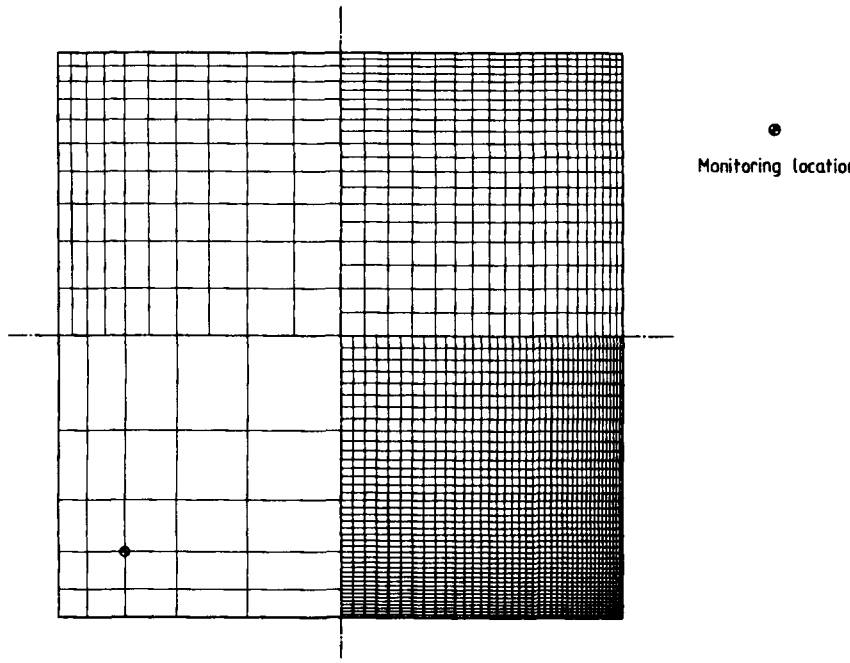


Figure 8. Segments of the first four grids (one quarter of each)

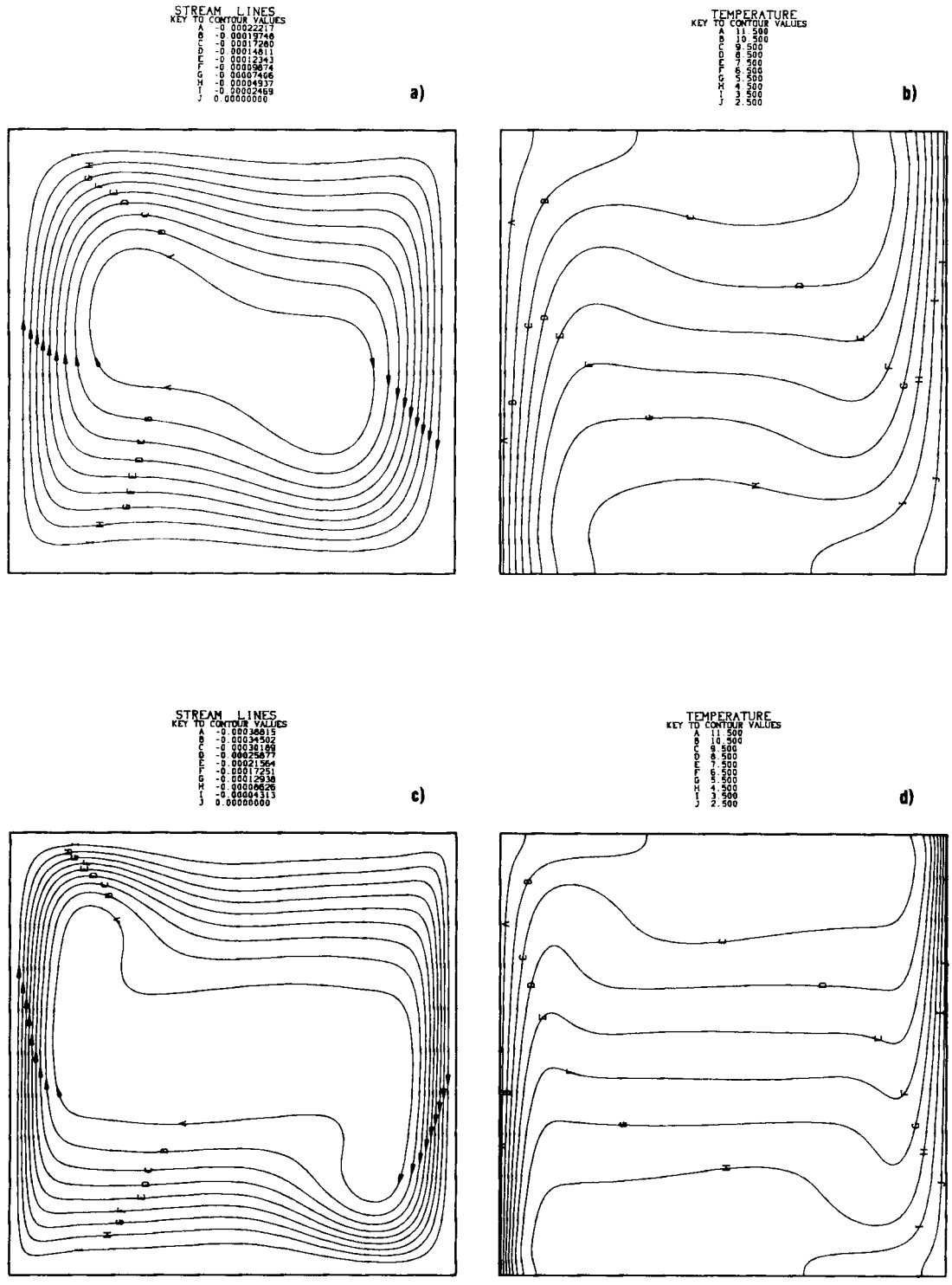


Figure 9. Predicted streamlines and isotherms: (a), (b) $Ra = 10^5$, 320 × 320 CV grid; (c), (d) $Ra = 10^6$, 640 × 640 CV grid

Comparisons have shown that the higher resolution of the wall boundary layers achieved with non-uniform grids increases the accuracy of the solutions, although formally the second-order accuracy is lost when the grid becomes non-uniform. The accuracy of solutions on various grids (i.e. grid dependence) is checked by comparing the mean Nusselt numbers. The latter is defined as

$$\overline{Nu} = Q/Q_C, \tag{21}$$

where $Q$ is the actual heat flux across the cavity and $Q_C$ is the heat flux that would result from pure conduction:

$$Q_C = \frac{\mu}{Pr}\frac{T_H - T_C}{L}H. \tag{22}$$

The heat flux $Q$ may be calculated by summing the convection and diffusion fluxes through the CV faces along any grid line at $x$ = constant. In the FV method used here, owing to its inherent conservativeness, it is equal (to within the accuracy determined by the convergence criterion) to the wall heat flux. The latter is determined by the difference in temperatures at the wall and at the centres of the near-wall CVs (see equation (8) and Figure 1). It should be noted that some authors (including de Vahl Davis[1]) use different formulae for the calculation of the temperature gradient at the wall when evaluating $\overline{Nu}$ from the numerical solution than those actually used to obtain that solution (usually higher-order expressions are used for $\overline{Nu}$). However, the only consistent expression is the one used in the solution of the temperature equation, since it defines the boundary condition for the solution.

Local and average Nusselt numbers were calculated for the cold and hot walls; these were identical to six significant figures, consistent with the convergence criterion used. Note that the width $\delta x$ across which the temperature gradient is calculated is half the near-wall mesh size; for the 640 × 640 grid this distance amounts to only 1/2980 of the cavity width.

Figures 10(a)–10(c) show the predicted mean Nusselt numbers as a function of the number of CVs for the three Rayleigh numbers. For $Ra = 10^5$ and $10^6$, results on both uniform and non-uniform grids are shown. Convergence towards the (same) grid-independent values is obvious in all cases. However, solutions on non-uniform grids are more accurate. Obviously, the accuracy is strongly dependent on the near-wall grid spacing. The non-uniform grid with 10 × 10 CV has the same near-wall $\delta x$ as the uniform 20 × 20 CV grid; surprisingly, the calculated $\overline{Nu}$-value on the coarsest non-uniform grid is for $Ra = 10^5$ more accurate than the value obtained on the uniform 20 × 20 CV grid. In all cases the non-uniform grid results are more accurate than the results on a uniform grid with twice as many CVs in each direction; thus one level of grid refinement is saved.

For $Ra = 10^4$ the desired accuracy was achieved on a 160 × 160 CV grid. One further refinement was necessary for $Ra = 10^5$, and one even more for $Ra = 10^6$. This is due to the fact that the wall boundary layers become thinner as $Ra$ increases, thus requiring finer grids for their resolution.

Apart from the average Nusselt number, the following quantities were also monitored:

(1) velocity components $U_{mon}$, $V_{mon}$ and temperature $T_{mon}$ at the reference location, indicated in Figure 8
(2) the maximum horizontal velocity component $U_{max}$ in the vertical midplane $x = L/2$ and its location $y_{max}$
(3) the maximum vertical velocity component $V_{max}$ in the horizontal midplane $x = H/2$ and its location $x_{max}$
(4) the maximum value of the local Nusselt number on the cold wall, $Nu_{max}$ and its position $y_{Nu}$.

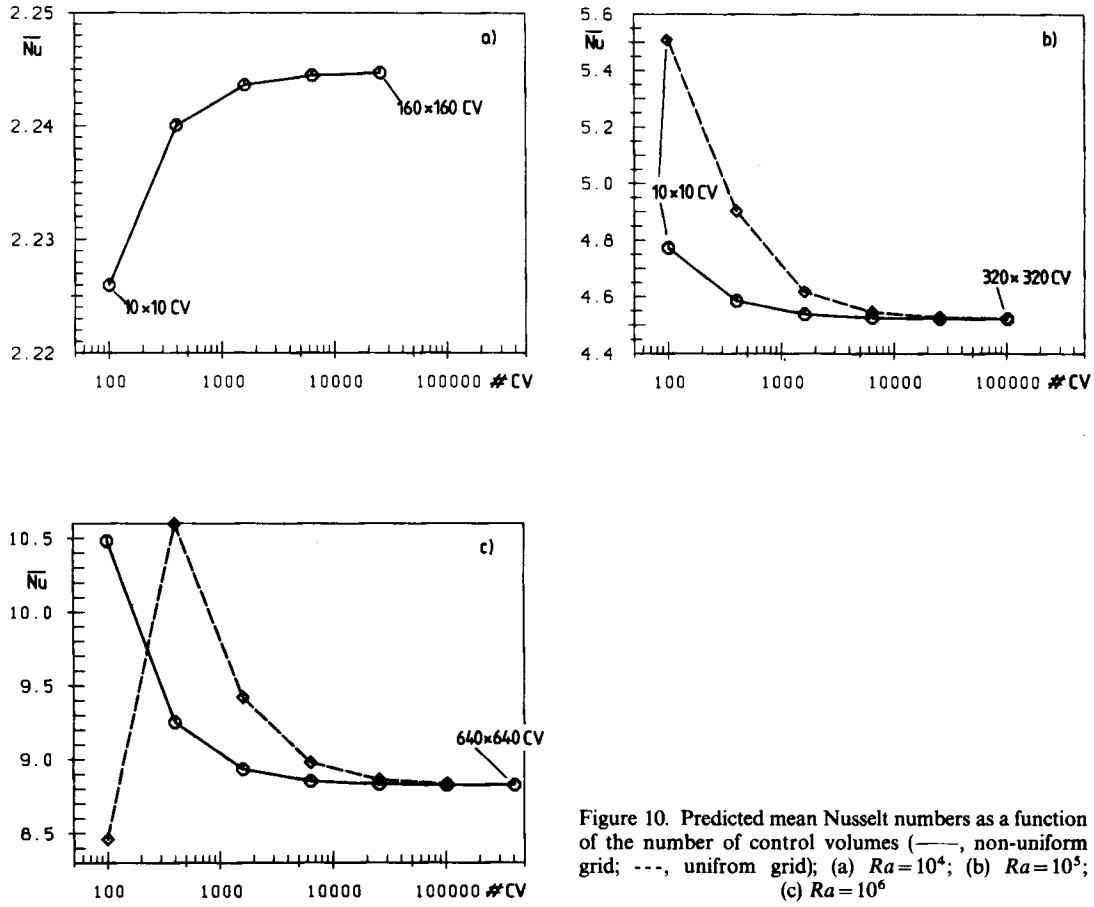


Figure 10. Predicted mean Nusselt numbers as a function of the number of control volumes (——, non-uniform grid; ---, unifrom grid); (a) $Ra=10^4$; (b) $Ra=10^5$; (c) $Ra=10^6$

The above reference location lies in a corner of four CVs on all grids, and the values there are obtained by bilinear interpolation (see Table III). Owing to the fact that computing points on various grids do not coincide, such a location is found to be the best choice; the same interpolation is applied on all grids and its accuracy is consistent with the discretization accuracy. Also, the two centrelines do not pass through the computational points but run along the CV faces; hence the velocity values there are obtained by linear interpolation. $Nu_{max}$ is the maximum value calculated at a wall boundary node. As the accuracy of the solution increases with grid refinement, the indicated value becomes closer to the actual maximum; on the finest grids the $Nu$-values at neighbour nodes differed from the maximum by less than 0·0025%. The $x$- and $y$-co-ordinates are normalized with the cavity width $L$, and the velocities are normalized with the diffusion velocity, defined as

$$V_{diff} = \frac{\mu}{Pr\rho L}. \tag{23}$$

Note that the monitoring locations on uniform and non-uniform grids do not correspond to the same physical location; hence the values recorded there cannot be compared.

Table III. Monitored values as predicted on various grids for various $Ra$ numbers: (a) $Ra = 10^4$, non-uniform grid; (b) $Ra = 10^5$, uniform grid; (c) $Ra = 10^5$, non-uniform grid; (d) $Ra = 10^6$, uniform grid; (e) $Ra = 10^6$, non-uniform grid

(a)

| Grid: | 10 × 10 | 20 × 20 | 40 × 40 | 80 × 80 | 160 × 160 | 320 × 320 | 640 × 640 |
|---|---|---|---|---|---|---|---|
| $U_{mon}$ | 5·97104 | 5·95915 | 5·93957 | 5·93388 | 5·93242 | — | — |
| $V_{mon}$ | 4·59770 | 4·53688 | 4·51889 | 4·51509 | 4·51417 | — | — |
| $T_{mon}$ | 8·10404 | 8·09741 | 8·09437 | 8·09341 | 8·09315 | — | — |
| $U_{max}$ | 15·0954 | 15·8602 | 16·0955 | 16·1630 | 16·1759 | — | — |
| $y_{max}$ | 0·83666 | 0·81551 | 0·82827 | 0·82246 | 0·82551 | — | — |
| $V_{max}$ | 18·1414 | 19·1925 | 19·5303 | 19·6082 | 19·6242 | — | — |
| $x_{max}$ | 0·08382 | 0·09944 | 0·12779 | 0·12261 | 0·12009 | — | — |
| $Nu_{max}$ | 3·6262 | 3·5585 | 3·5373 | 3·5326 | 3·5313 | — | — |
| $y_{\overline{Nu}}$ | 0·83665 | 0·86123 | 0·85108 | 0·85667 | 0·85399 | — | — |
| $\overline{Nu}$ | 2·22596 | 2·24003 | 2·24360 | 2·24446 | 2·24468 | — | — |

(b)

| Grid: | 10 × 10 | 20 × 20 | 40 × 40 | 80 × 80 | 160 × 160 | 320 × 320 | 640 × 640 |
|---|---|---|---|---|---|---|---|
| $U_{mon}$ | 25·7400 | 25·9937 | 25·4630 | 25·3120 | 25·2752 | 25·2664 | — |
| $V_{mon}$ | −0·2312 | 0·15719 | 0·41786 | 0·47067 | 0·47940 | 0·48079 | — |
| $T_{mon}$ | 4·37013 | 4·60811 | 4·71222 | 4·73885 | 4·74567 | 4·74739 | — |
| $U_{max}$ | 33·4980 | 34·5813 | 34·7396 | 34·7499 | 34·7398 | 34·7414 | — |
| $y_{max}$ | 0·85000 | 0·87500 | 0·86250 | 0·85625 | 0·85312 | 0·85468 | — |
| $V_{max}$ | 74·7740 | 66·4046 | 68·8438 | 68·5600 | 68·6465 | 68·6187 | — |
| $x_{max}$ | 0·05000 | 0·07500 | 0·06250 | 0·06875 | 0·06562 | 0·06719 | — |
| $Nu_{max}$ | 9·3456 | 9·1349 | 8·1507 | 7·8289 | 7·7468 | 7·7269 | — |
| $y_{\overline{Nu}}$ | 0·95000 | 0·97500 | 0·93750 | 0·91875 | 0·92253 | 0·91718 | — |
| $\overline{Nu}$ | 5·50768 | 4·90271 | 4·61653 | 4·54516 | 4·52751 | 4·52310 | — |

(c)

| Grid: | 10 × 10 | 20 × 20 | 40 × 40 | 80 × 80 | 160 × 160 | 320 × 320 | 640 × 640 |
|---|---|---|---|---|---|---|---|
| $U_{mon}$ | 22·8893 | 22·5537 | 22·3195 | 22·2560 | 22·2397 | 22·2355 | — |
| $V_{mon}$ | 6·18282 | 5·75680 | 5·45072 | 5·34922 | 5·32148 | 5·31465 | — |
| $T_{mon}$ | 5·25255 | 5·38785 | 5·42129 | 5·42945 | 5·43149 | 5·43198 | — |
| $U_{max}$ | 33·6327 | 34·4483 | 34·6324 | 34·7132 | 34·7342 | 34·7385 | — |
| $y_{max}$ | 0·83665 | 0·86124 | 0·85106 | 0·85665 | 0·85399 | 0·85535 | — |
| $V_{max}$ | 63·5864 | 68·8421 | 68·0898 | 68·5383 | 68·6239 | 68·6359 | — |
| $x_{max}$ | 0·08381 | 0·06563 | 0·07315 | 0·06902 | 0·06701 | 0·06602 | — |
| $Nu_{max}$ | 9·0589 | 8·0665 | 7·8018 | 7·8289 | 7·7252 | 7·7214 | — |
| $y_{\overline{Nu}}$ | 0·97499 | 0·93436 | 0·92684 | 0·91444 | 0·91660 | 0·91767 | — |
| $\overline{Nu}$ | 4·77266 | 4·58407 | 4·53727 | 4·52556 | 4·52261 | 4·52188 | — |

(d)

| Grid: | 10 × 10 | 20 × 20 | 40 × 40 | 80 × 80 | 160 × 160 | 320 × 320 | 640 × 640 |
|---|---|---|---|---|---|---|---|
| $U_{mon}$ | 57·6861 | 51·2769 | 52·1035 | 51·2836 | 51·0290 | 50·9677 | — |
| $V_{mon}$ | −12·0221 | 1·85373 | 0·86255 | 0·83833 | 0·84858 | 0·84958 | — |
| $T_{mon}$ | 4·74786 | 4·07203 | 4·34212 | 4·41893 | 4·43779 | 4·44263 | — |
| $U_{max}$ | 63·3419 | 63·2168 | 65·3710 | 64·9944 | 64·8659 | 64·8408 | — |
| $y_{max}$ | 0·95000 | 0·87500 | 0·86250 | 0·85625 | 0·85312 | 0·85156 | — |
| $V_{max}$ | 194·532 | 242·719 | 223·412 | 218·312 | 219·861 | 220·438 | — |
| $x_{max}$ | 0·05000 | 0·02500 | 0·03750 | 0·03125 | 0·04062 | 0·03906 | — |
| $Nu_{max}$ | 12·351 | 20·959 | 20·900 | 18·638 | 17·810 | 17·606 | — |
| $y_{\overline{Nu}}$ | 0·95000 | 0·97500 | 0·98750 | 0·96874 | 0·96562 | 0·96094 | — |
| $\overline{Nu}$ | 8·46097 | 10·5976 | 9·42167 | 8·97719 | 8·86302 | 8·83459 | — |

Table III. (Continued)

(e)

| Grid: | 10 × 10 | 20 × 20 | 40 × 40 | 80 × 80 | 160 × 160 | 320 × 320 | 640 × 640 |
|---|---|---|---|---|---|---|---|
| $U_{mon}$ | 55·6177 | 56·4353 | 56·8531 | 57·0232 | 57·0729 | 57·0857 | 57·0889 |
| $V_{mon}$ | −15·387 | −6·7214 | −4·4433 | −3·9898 | −3·8843 | −3·8586 | −3·8522 |
| $T_{mon}$ | 3·54255 | 4·03081 | 4·12825 | 4·15241 | 4·15852 | 4·16006 | 4·16045 |
| $U_{max}$ | 56·5397 | 63·3498 | 64·2963 | 64·6276 | 64·7885 | 64·8249 | 64·8340 |
| $y_{max}$ | 0·91619 | 0·86124 | 0·85106 | 0·85665 | 0·84850 | 0·84990 | 0·85036 |
| $V_{max}$ | 247·411 | 225·384 | 218·163 | 220·497 | 220·641 | 220·507 | 220·473 |
| $x_{max}$ | 0·02500 | 0·03656 | 0·04303 | 0·03947 | 0·03775 | 0·03859 | 0·03887 |
| $Nu_{max}$ | 22·815 | 20·627 | 18·374 | 17·743 | 17·587 | 17·549 | 17·540 |
| $y_{Nu}$ | 0·97500 | 0·98844 | 0·97041 | 0·96053 | 0·96225 | 0·96141 | 0·96098 |
| $\overline{Nu}$ | 10·4798 | 9·25287 | 8·93128 | 8·85148 | 8·83170 | 8·82677 | 8·82554 |

Table IV. Grid-independent results estimated by extrapolation

| $Ra$ | $U_{mon}$ | $V_{mon}$ | $T_{mon}$ | $U_{max}$ | $V_{max}$ | $Nu_{max}$ | $\overline{Nu}$ |
|---|---|---|---|---|---|---|---|
| $10^4$ | 5·93193 | 4·51387 | 8·09307 | 16·1802 | 19·6295 | 3·53087 | 2·24475 |
| $10^5$ | 22·2341 | 5·31237 | 5·43215 | 34·7399 | 68·6396 | 7·72013 | 4·52164 |
| $10^6$ | 57·0901 | −3·8501 | 4·16057 | 64·8367 | 220·461 | 17·536 | 8·82513 |

All quantities are seen to converge monotonically towards a grid-independent value. It is interesting to note that the mean Nusselt number for $Ra = 10^4$ increases with grid refinement, while the maximum value decreases; for other Rayleigh numbers both $\overline{Nu}$ and $Nu_{max}$ decrease with grid refinement.

We observe that the difference between the values obtained on grids $k$ and $k-1$ is about a quarter of the difference between grids $k-1$ and $k-2$. This is approximately valid for all variables on all but the coarsest grids. Using this reduction rate as the basis for extrapolation, we arrive at more accurate ('grid-independent') values

$$\phi = \phi_k + \tfrac{1}{3}(\phi_k - \phi_{k-1}). \tag{24}$$

The above expression corresponds to the Richardson extrapolation for second-order schemes. The CDS scheme for convection used here is of second order on both uniform and non-uniform grids; the diffusion approximation is of second order only on uniform grids, and on non-uniform grids it has a first-order truncation error term multiplied by $1-\eta$. Since $\eta$ tends to unity as the grid gets finer, the overall discretization can be considered to be of second order. Extrapolated values, calculated from the above equation and the results of the two finest grids, are summarized in Table IV. Approximately the same values are obtained when the other two grids are used (except for the three coarsest ones).

That the above extrapolation is accurate can be concluded by comparing the values obtained from the results of calculations on uniform and non-uniform grids. For example, extrapolated average Nusselt numbers for $Ra = 10^5$ and $10^6$ differ only in the sixth significant figure (less than 0·0002%), which is the limit of the accuracy specified by the convergence criterion employed in

the calculations. This also certifies that the present solution method does converge to the unique solution irrespective of the kind of grid used. The results of calculations on the finest (non-uniform) grids differ from the estimated grid-independent values by less than 0·01%, which is the believed accuracy of the present computations.

Knowing the grid-independent results, solution errors on various grids can be estimated by subtracting the corresponding values of Table III from those of Table IV. Figures 11(a)–11(d)

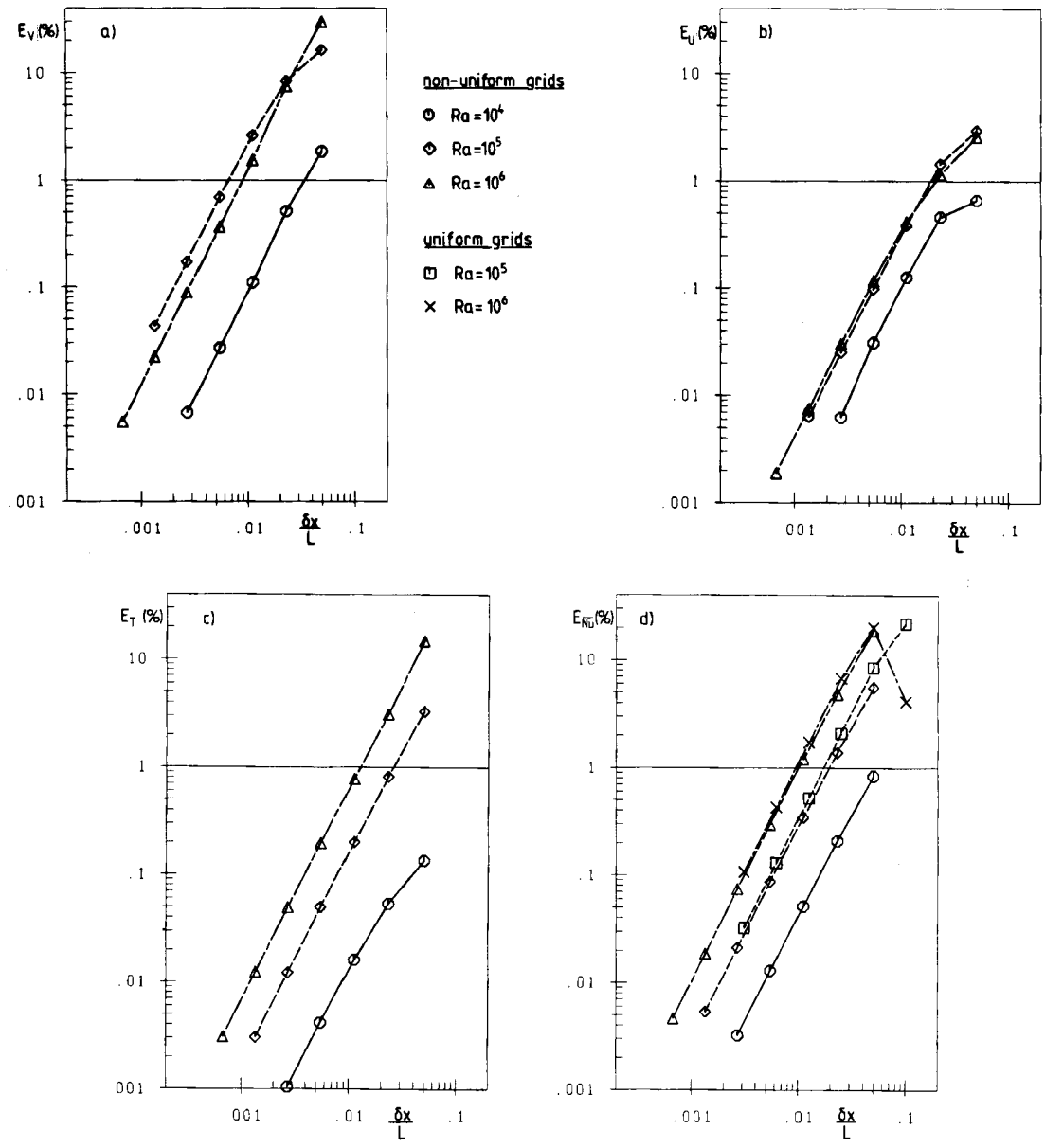


Figure 11. Estimated solution errors as a function of grid size for various $Ra$ numbers: (a) $V_{mon}$; (b) $U_{mon}$; (c) $T_{mon}$; (d) $\overline{Nu}$

show the errors for $U_{mon}$, $V_{mon}$, $T_{mon}$ and $\overline{Nu}$ plotted against the smallest $\delta x$ as a representative grid spacing, using a logarithmic scale. All curves indicate a slope of around 2 (2·2 seems to be the best fit). There is little difference between the curves for uniform and non-uniform grids (the uniform grid ones seem to be slightly steeper for larger values of $\delta x$). Thus the second order of the solution method is retained on non-uniform grids as well. However, the accuracy of the results obtained on non-uniform grids is almost one order of magnitude better than on uniform grids having the same number of nodes (see Figure 11(d)). Accuracy is obviously determined by the mesh size in regions of high variation of the dependent variables — in this case near walls; the fact that the grid is expanding does not seem to affect the results appreciably.

Compared with the results of de Vahl Davis,[1] the values of Table IV, which are accurate to within approximately 0·001%, show small discrepancies. These are, however, well within the accuracy estimates given by de Vahl Davis. For example, for $\overline{Nu}$ he estimated the bounds to be 0·2%, 0·3% and 1·0% for Rayleigh numbers $10^4$, $10^5$ and $10^6$ respectively; the difference from our results is 0·08%, 0·06% and 0·2% respectively. It is, though, interesting to note that de Vahl Davis gives different bench-mark solutions for the average Nusselt numbers at the cavity centre and at the walls (0·2% difference at $Ra = 10^6$), although these — even when a non-conservative solution method is used — should become identical as $\delta x$ tends to zero. This is believed to be due to the inconsistency of $Nu$ evaluation, as noted above.

The present calculations on such fine grids were only made possible by application of the multigrid scheme presented in the previous section. Its efficiency can be assessed by comparing the computing times and numbers of iterations required to obtain solutions of the same accuracy and starting from the same initial guess with and without multigrid. Table V shows the numbers of iterations required for convergence on various grids and Table VI the corresponding computing times for the two methods and $Ra = 10^5$. Single-grid calculations were pursued to convergence only up to the 80 × 80 CV grid, since the computing times for finer grids would have been excessively long (see the estimates in Table VI). 80 × 80 CV single-grid calculations take already about 14 times longer than when multigrid is employed (the same computer code is used, with the MG switch set on or off). The estimated factor for the 320 × 320 CV grid is approximately 100. The computing time for the multigrid method varies roughly proportionally to the

Table V. Number of iterations required for convergence on the finest grid by the multigrid and single-grid method for $Ra = 10^5$

| Grid: | 10 × 10 | 20 × 20 | 40 × 40 | 80 × 80 | 160 × 160 | 320 × 320 |
|---|---|---|---|---|---|---|
| SG | 53 | 83 | 171 | 406 | 1200* | 4000* |
| MG | 53 | 56 | 41 | 25 | 22 | 29 |

* Estimated.

Table VI. Computing time required for convergence on the finest grid by the multigrid and single-grid method for $Ra = 10^5$

| Grid: | 10 × 10 | 20 × 20 | 40 × 40 | 80 × 80 | 160 × 160 | 320 × 320 |
|---|---|---|---|---|---|---|
| SG | 0·80654 | 4·346 | 35·56 | 451·106 | 5400* | 65000* |
| MG | 0·80654 | 3·3315 | 11·502 | 32·457 | 131·96 | 690·8 |

* Estimated.

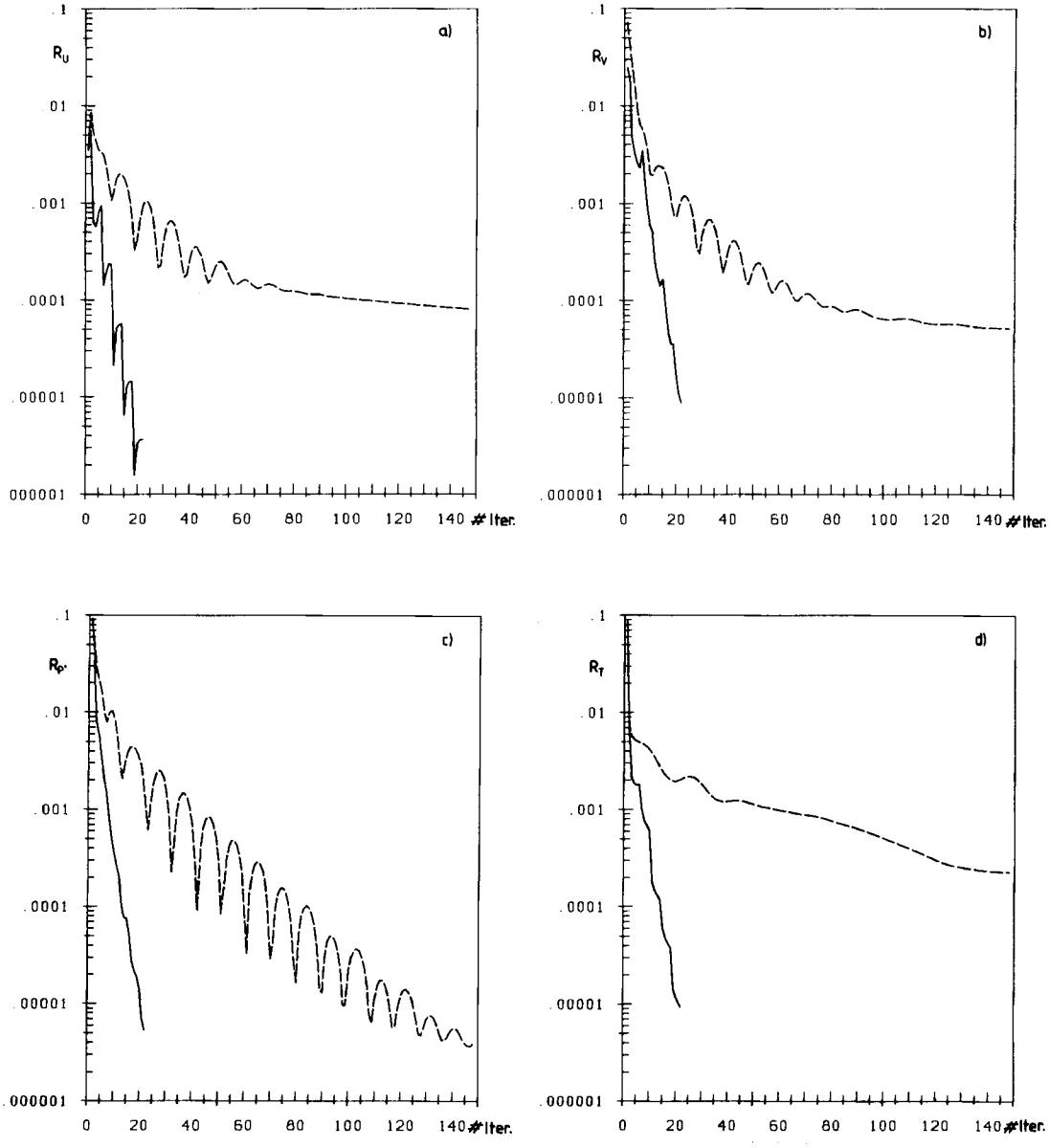


Figure 12. Residuals on a 160 × 160 CV grid as a function of the number of fine grid iterations (——, multigrid; - - -, single grid): (a) $U$; (b) $V$; (c) $P'$; (d) $T$

number of CVs (number of iterations approximately constant on finer grids), while for the single-grid method it is proportional to the square of the number of CVs (number of iterations increasing linearly as the grid is refined). It should be noted that in both cases the solution on the finest grid starts from the extrapolated solution on the next coarser grid; the cost of obtaining this solution is not included in the computing times of Table VI. Similar relations are valid for other Rayleigh numbers; lower *Ra*-values would however require less, and higher more iterations.

If the convergence criterion were made tighter, the ratios of computing times for the two methods would have been even more favourable for the multigrid version. This is apparent from Figures 12(a)–12(d), which present the residual norms on a 160 × 160 CV grid as a function of the number of iterations performed. In the multigrid calculations the residuals fall at a constant rate for all variables (the peaks after one V-cycle is finished are believed to be due to interpolation errors introduced when changing grids and to the coupling and non-linearity of equations). On the other hand, in the single-grid method the residuals fall fast only at the beginning of the iteration process, their change becoming slower and slower as the process continues. This behaviour becomes more pronounced as the grid gets finer, while in the case of multigrid the rate of convergence remains about the same (see Table V).

## 5. CONCLUSIONS

The multigrid method presented in this paper provides for a fast convergence of the finite volume solution procedure with collocated grids. It has been applied to the natural convection flow in a square cavity at Rayleigh numbers $10^4$, $10^5$ and $10^6$, and enabled very accurate solutions to be obtained on grids as fine as 640 × 640 control volumes. The results may be summarized as follows.

1. The solution method used converges monotonically to a unique grid-independent solution as the grid is refined.
2. With the central differencing scheme employed for both convection and diffusion fluxes the solution method shows second-order convergence for both uniform (square) and non-uniform (expansion ratio up to 1·4, aspect ratio up to 4) grids.
3. The accuracy of the solutions is greatly improved by employing non-uniform grids, with smaller spacing near walls; typically one level of grid refinement can thus be saved.
4. The results presented here are believed to be accurate to within 0·01%. Earlier published bench-mark solutions of the same problem differ from the present ones by up to 0·2% in Nusselt number and up to 1·6% in maximum velocity (at $Ra = 10^6$; for lower values of $Ra$ the differences are smaller than 0·07% for all quantities).
5. Grid-independent results are estimated by extrapolation. Values obtained by extrapolation from the results of uniform and non-uniform grids agree to within 0·0002%; these are hence believed to be accurate to within 0·001%.
6. The multigrid version of the solution method requires only about 1% of the computing time needed by the standard version on a 320 × 320 CV grid. The computing time requirement increases linearly as the grid is refined, as opposed to the quadratic increase in the standard method.

The present multigrid method can easily be extended to non-orthogonal grids and to the solution of additional equations (e.g. for the swirl velocity, turbulence quantities, etc.). Such extensions are presently under way.

### ACKNOWLEDGEMENTS

The authors wish to acknowledge the contribution of M. Barcus, C. Becker and M. Rüger to the development of the multigrid method described above. Support of the Deutsche Forschungsgemeinschaft and Regionales Rechenzentrum Erlangen is also greatly appreciated.

## REFERENCES


1. G. de Vahl Davis, 'Natural convection of air in a square cavity: a bench mark numerical solution', *Int. j. numer. methods fluids*, **3**, 249–264 (1983).
2. A. Brandt, 'Multi-level adaptive computations in fluid dynamics', *AIAA Paper 79-1455*, 1979.
3. S. P. Vanka, 'Block-implicit multigrid solution of Navier–Stokes equations in primitive variables', *J. Comput. Phys.*, **65**, 138–158 (1986).
4. S. Sivaloganathan and G. J. Shaw, 'A multigrid method for recirculating flows', *Int. j. numer. methods fluids*, **8**, 417–440 (1988).
5. E. Dick, 'A multigrid method for steady incompressible Navier–Stokes equations based on partial flux splitting', *Int. j. numer. methods fluids*, **9**, 113–120 (1989).
6. M. Barcus, M. Perić and G. Scheuerer, 'A control volume based full multigrid procedure for the prediction of two-dimensional, laminar, incompressible flows', in M. Deville (ed.), *Notes on Numerical Fluid Mechanics, Vol. 20*, Vieweg, Braunschweig, 1988, pp. 9–16.
7. C. Becker, J. H. Ferziger, M. Perić and G. Scheuerer, 'Finite volume multigrid solutions of the two-dimensional incompressible Navier–Stokes equations', in W. Hackbusch (ed.), *Notes on Numerical Fluid Mechanics, Vol. 23*, Vieweg, Braunschweig, 1988, pp. 37–47.
8. M. Perić, M. Rüger and G. Scheuerer, 'A finite volume multigrid method for calculating turbulent flows', *Proc. 7th Symp. on Turbulent Shear Flows*, Stanford, CA, 1989, pp. 7.3.1–7.3.6.
9. G. de Vahl Davis, and I. P. Jones, 'Natural convection in a square cavity: a comparison exercise', *Int. j. numer. methods fluids*, **3**, 227–248 (1983).
10. M. Perić, R. Kessler and G. Scheuerer, 'Comparison of finite-volume numerical methods with staggered and colocated grids', *Comput. Fluids*, **16**, 389–403 (1988).
11. P. K. Khosla and S. G. Rubin, 'A diagonally dominant second-order accurate implicit scheme', *Comput. Fluids*, **2**, 207–209 (1974).
12. H. L. Stone, 'Iterative solution of implicit approximations of multi-dimensional partial differential equations', *SIAM J. Numer. Anal.*, **5**, 530–558 (1968).
13. S. V. Patankar and D. B. Spalding, 'A calculation procedure for heat, mass and momentum transfer in three-dimensional parabolic flows', *Int. J. Heat Mass Transfer*, **15**, 1787–1806 (1972).